Article:

Brereton, B.A., Hait, S., Yagmur, A. et al. (Accepted: 2026) Tailoring Ultrathin Magnetic Multilayers at Terraced Topologically Insulating Interfaces for Perpendicularly Magnetized Domains. Physical Review Materials. ISSN: 2475-9953 (In Press)

Tailoring Ultrathin Magnetic Multilayers at Terraced Topologically Insulating Interfaces for Perpendicularly Magnetized Domains: Supplementary Material

Benjamin A. Brereton[1,2,3], Soumyarup S. Hait[1], Ahmet Yagmur[1], Christy Kinane[2], Francesco Maccherozzi[3], Michele Conroy[4], Satoshi Sasaki[1], Sarnjeet S. Dhesi[3], Sean Langridge[2], Thomas A. Moore[1], and Christopher H. Marrows[1]

[1]School of Physics and Astronomy, University of Leeds, Leeds LS2 9JT, UK
[2]ISIS Neutron and Muon Source, STFC Rutherford Appleton Laboratory, Harwell Science and Innovation Campus, Chilton, Oxfordshire OX11 0QX, UK
[3]Diamond Light Source, Harwell Science and Innovation Campus, Chilton, Oxfordshire OX11 0DE, UK
[4]Department of Materials, Imperial College London, Exhibition Road, London SW7 2AZ, UK

May 20, 2026

1. Measurements

1.1 X-ray Reflectivity Measurements

X-ray experiments were performed using a Bruker D8 discovery X-ray diffractometer with a Cu K-α X-ray source. Samples were aligned for specular reflection for XRR at $2\theta = 1^\circ$ grazing incidence and for XRD measurements using the $2\theta = 41.69^\circ$ Al_2O_3 substrate diffraction peak. Both measurements were performed in the standard $\theta/2\theta$ geometry. SLD distributions on silicon were simulated and fitted to the XRR data using the GenX software package [2]. Where X-rays were co-fitted with neutrons, the Refl1D python library was used [4].

1.2 High-Angle Annular Dark Field STEM (HAADF STEM)

The cross-section lamella for STEM imaging was prepared using a dual-beam focused ion beam integrated scanning electron microscope (Thermo-Fisher Scientific FEI G5 CX). After electron-beam deposition of C and Pt on the surface, the samples were thinned to electron transparency. The STEM imaging was carried out using a Thermo-Fisher Scientific double-tilt STEM holder in the Thermo-Fisher Scientific FEI probe-corrected monochromated XFEG Spectra 300. The microscope was operated at 300 kV. The convergence angle was 30 mrad, and the collection angle for ADF images was 52–200 mrad using the HAADF detector. All STEM images were processed using Thermo Fisher Scientific drift corrected frame integration Velox software to correct for drift/scan distortion.

1.3 SQUID-VSM and MOKE Microscopy

All measurements were conducted on a Quantum Design MPMS-3 SQUID-VSM magnetometer. Samples were demagnetized and measured through -1 to 1 T forward and reverse field sweeps. SQUID signals were corrected by subtracting a linear diamagnetic background from Al_2O_3/Bi_2Se_3, correcting for trapped flux in the superconducting coils by correcting H using a Pd reference sample of known susceptibility and dividing by an IP or OOP filling factor. Effective anisotropies were calculated by calculating the difference in out-of-plane and in-plane, $M(H)$ integrals with respect to H.

All MOKE measurements were conducted in the polar configuration for OOP magnetic sensitivity on a Kerr microscope with white LED source. Signals were corrected for Faraday components and thermal drift of the LED. The magnetic field was applied using an air core coil to avoid magnetic remanance from a permanent pole piece, and samples were measured up to a maximum applied field of $\pm$30 mT. Domains were observable being in the lower limit of what is optically resolvable as shown in Fig. 1. A domain periodicity on the Si reference sample of $\lambda_{\mathrm{FFT}/2} \sim 600$ nm was observed.

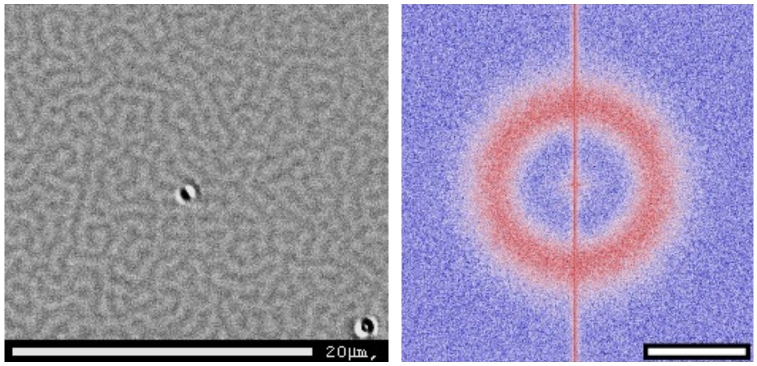

Figure 1: Polar MOKE image of $Si/SiO_2/Ta$(5.0 nm)/MML reference sample. FFT is shown inset with scale bar corresponding to $1\mu m^{-1}$

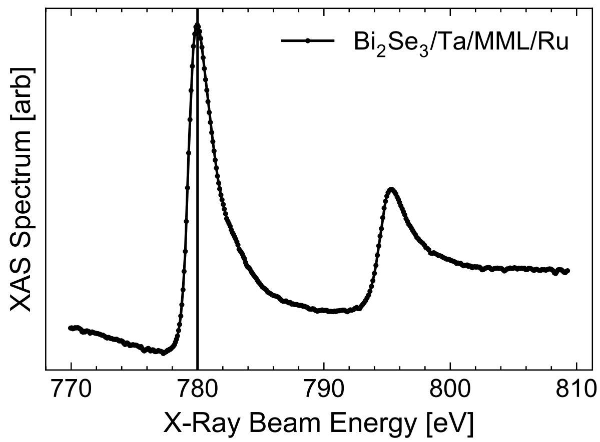

Figure 2: Example Co XAS pattern of multilayer on Bi_2Se_3 with 1 nm Ru cap. Line shows alignment to Co L_3 edge.

1.4 X-ray Photoemission Electron Microscopy

All XMCD X-PEEM measurements were conducted at the I06 beamline at the Diamond Light Source. Images were collected at the Co L_3 edge at room temperature and under a 15 kV bias. These were taken with a thin 1 nm Ru cap shortly after growing to maximise counts from photoemission. Little/no evidence of peak-splitting or shouldering implies sample remains unoxidised despite the thin cap. Multiple images using both X-ray helicities were taken, subtracted, drift-corrected and averaged over. X-ray absorption spectroscopy (XAS) measurements imply minimal oxidation of Co under the 1 nm Ru capping due to a lack of any noticeable shoulder appearing on the peaks in the XAS spectra as shown in Fig.

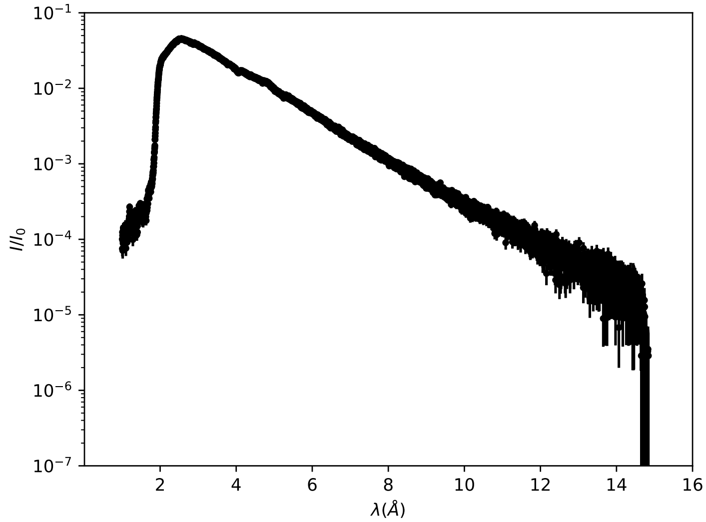

Figure 3: Transmission statistics used for data reduction showing distribution of time-of-flight detected neutrons.

2. The vanishing total XMCD signal under zero applied field is consistent with maze domain formation with equal areas of up and down domains.

2. Polarized Neutron Reflectometry

2.1 Neutron Measurements

All PNR measurements were conducted on the POLREF reflectometer at the ISIS Neutron and Muon Source. Measurements are time of flight, polarised in-plane and taken in specular geometries. Reflected intensities in neutron channels R_+ and R_- were collected.

Each reflectivity curve involved measurements at $2\theta = 0.1°, 1.2°, 2.3°$ at 1, 2 and 8 hours respectively. To ensure good counting statistics samples were prepared as 2 inch diameter wafers. The in-plane external magnetic field was applied using a room-temperature magnet from 0.7 T decreasing to near remanance. Measurements must be conducted at a minimum of 10 mT or higher to maintain reliable beam polarisation. Care was taken to obtain good transmission statistics over mutliple hours as shown in Fig. 3.

Bi_2Se_3/Ta(2.0 nm)/MML
$\chi^2 = 2.84$

Bi_2Se_3/Mo(1.0 nm)/MML
$\chi^2 = 2.87$

Bi_2Se_3/MML/Pt
$\chi^2 = 5.97$

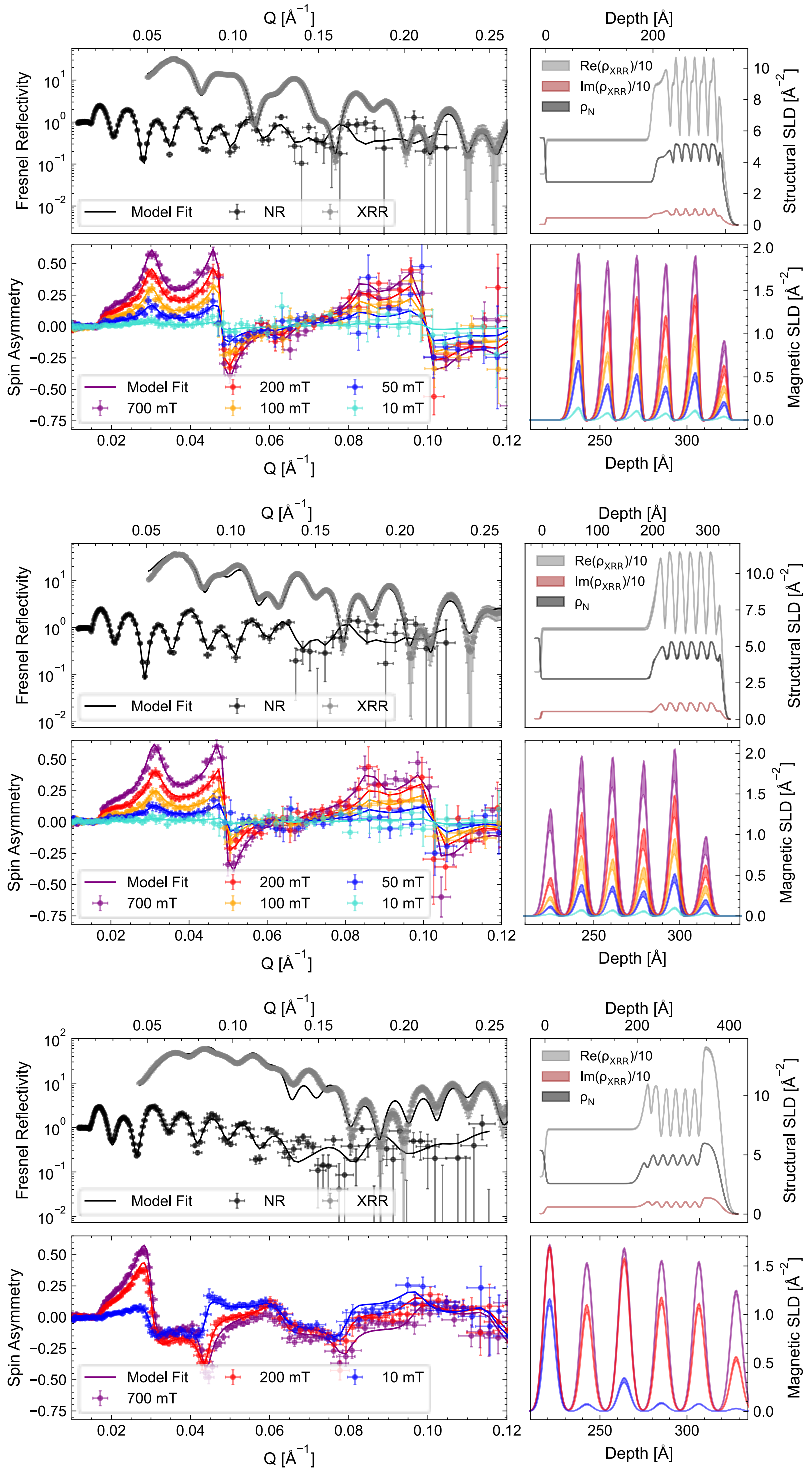

Figure 4: PNR & XRR curves fitted by a shared multilayer slab model for, from top to bottom, a Ta(2.0 nm) buffer, Mo(1.0 nm) buffer and no buffer. Non-magnetic neutron and X-ray components are shown in (a) with magnetic polarized neutron spin asymmetry information shown in (b) as a function of an applied, in-plane field. Both are fitted by non-magnetic and magnetic scattering length density (SLD) distributions of which 1σ confidence intervals are shown in (c) and (d) respectively.

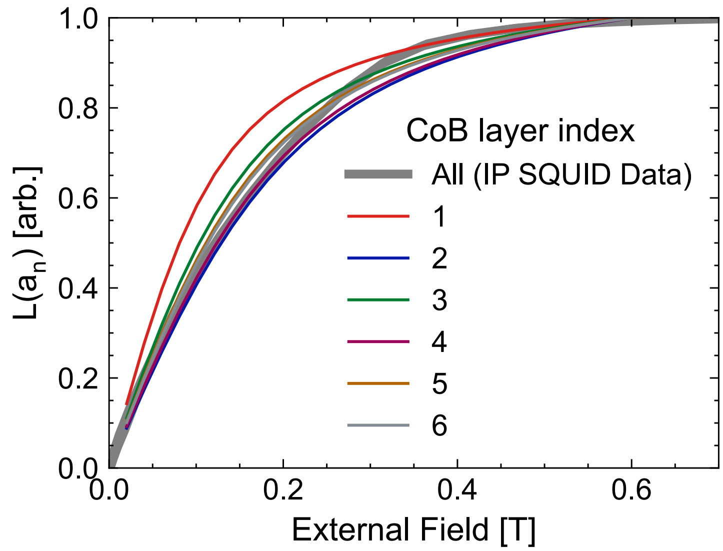

Figure 5: Modelled CoB layers' individual Langevin dependences in the Bi_2Se_3/Ta(2.0 nm)/MML structure compared to the stack-averaged SQUID magnetometry.

2.2 Slab Modelling

The data was simulated using the Refl1D Python library and fitted using the DREAM algorithm. 2 reflectivity measurements at each of 5 (3 for non-buffered and Ta(15 Å) buffer samples) fields alongside sample specific XRR curves were co-fitted. All models share the same structural parameters. The final model used modelled individual CoB layers with variable magnetisations idealised as 6 layer-by-layer Langevin functions. Note whilst these layers are magnetically independent they share thicknesses, densities and roughnesses. The combined X-ray, nuclear neutron and magnetic neutron SLDs are shown in figure 4 and the modelled IP Langevin relations compared to SQUID magnetometry are shown in figure 5. Shown in figure 6 are the chi-squared values for models of increasing complexity whilst fitting neutron data only. Whilst modelling the full multilayer as a single average magnetic layer obtains a satisfactory fit of $\chi^2 \sim 4$ for buffered samples, modelling these layers as individually resolvable results in an improvement in the final reduced chi-squared test statistic indicating we are weakly sensitive to this lengthscale. A phenomenological 'oxidation' parameter was introduced: modelled by decreasing the M_s of the topmost layer by a fraction, This was

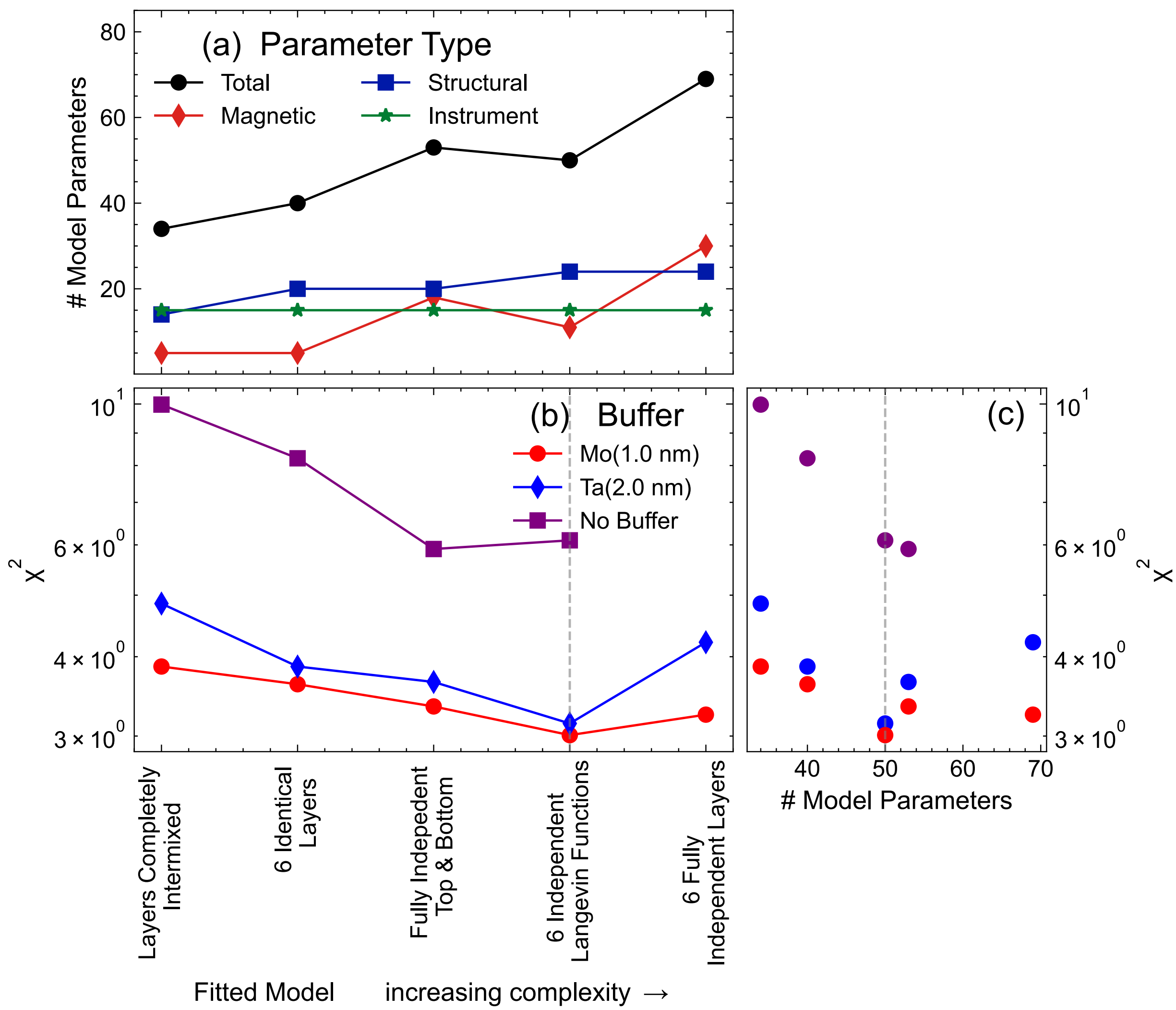

Figure 6: Comparison of the models used to fit neutron reflectivity data increasing in the complexity / freedom in magnetic modelling from left to right showing: (a) the number of parameters for each model by category; (b) The neutron χ^2 dependence on selected model and (c) the neutron χ^2 dependence as a function of increasing number of parameters. The dashed grey line denotes the final Langevin model used throughout and shown in Fig. 4 for the different buffers

found to be necessary to include otherwise the model would compensate by increasing H_k such that the layer would not saturate at 0.7 T and is necessary for fitting the features in spin asymmetry at $Q \sim 0.065\text{Å}^{-1}$. It is notable however when this oxidation parameter is large ($\sim$ 50%), the error in the extracted effective anisotropy of the topmost layer is greatly increased.

Structurally this can be improved further with the introduction of X-ray co-fitting. The X-rays' systematic errors, due to their much higher flux, tend to dominate the χ^2 dependence and hence the fitting, for which an additional 10 % error is included. Here the fully intermixed model only achieves $\chi^2 \sim 16$ whilst individual layers: $\chi^2 = 2.8$ for the Ta(2.0 nm) buffer. It should be noted the quality of the X-ray fit was improved dramatically when layer densities were allowed to take different values for neutrons and X-ray SLDs. Considering corresponding values usually lay within $\pm 5\%$ of each other this was not regarded as significant.

The fully intermixed model obtains $\chi^2 \sim 10$ where the heterostructure is grown without a buffer layer resulting in behaviour being anisotropic throughout the stack which improves to $\chi^2 = 6.1$ when modelling the interfacial layer perseverate. The weaker chi-squared dependence for buffered samples can hence be taken as a consequence of their uniform structure.

Further increasing the freedom and complexity in the fit model such that the magnetisation of each layer at each field is a completely free parameter does not improve the chi-squared suggesting too many parameters have been introduced for the model fitting to properly converge. This hence justifies coupling the layers magnetisation at each field under an effective magnetic 'stiffness' parameter, a_n related to $K_{\text{eff},n}$ and as the five magnetisations of any one layer at 5 fields are not independent of each other. Assuming the layers have full PMA we can approximate the effective anisotropy as the integral of the difference between modelled in-plane and measured out-of-plane curves:

$$K_{\text{eff},n} \approx \mu_0 \int_{H=0}^{H_K} \left(M_{\text{SQUID, OOP}} - M_s \mathcal{L}(a_n H) \right) \, dH \tag{1}$$

Looking at the magnetic parameter correlations in Figs. 7 & 8 informs us on whether pa-

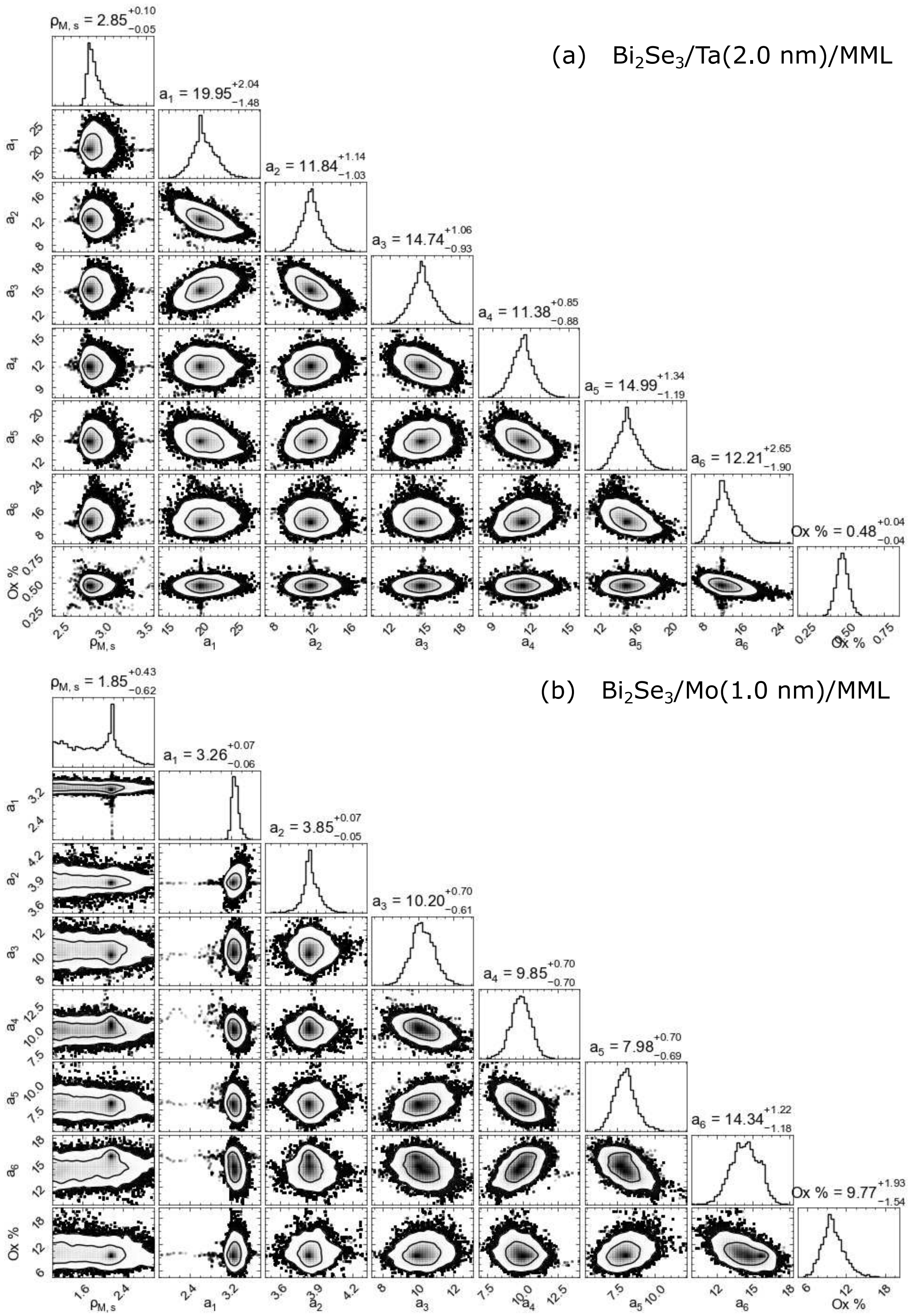

Figure 7: Bumps fit magnetic parameter correlations for Ta(2.0 nm) (a) and Mo(1.0) (b) buffers. Contour plots show both 68% and 95% confidence intervals. Plots created using the corner python package [1].

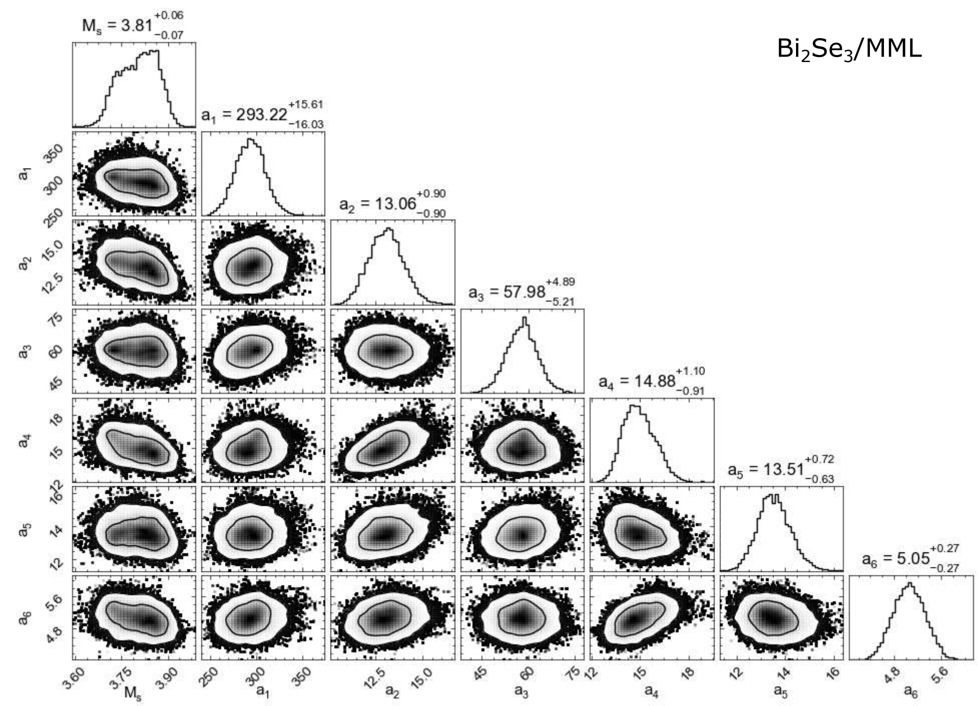

Figure 8: Bumps fit magnetic parameter correlations for sample without a buffer layer. Contour plots show both 68% and 95% confidence intervals. This sample has a 4 nm Pt cap and hence lacks an oxidation parameter. Plots created using the corner python package [1].

rameters are meaningful and independent. The majority of parameters appear uncorrelated, particularly for the non-buffered sample in Fig. 8. For the two buffered samples in Fig. 7 we notice weak to moderate correlation between the modelled a_n values for neighbouring FM layers indicating individual layer modelling is partially limited due to our statistics at high Q.

Neutron beams are known to typically possess a coherence length in the micron-scale, far exceeding the average Bi_2Se_3 terrace width for both wide and narrow Bi_2Se_3 terrace types. Hence we are able to assume the effective medium approximation applies and that in reality the presence of terracing from the Bi_2Se_3 will blur the multilayer features over the lengthscale of ~ 1 nm. This likely renders individual layers to be not fully resolvable regardless of model choice or statistics collected.

All models used can be found in the open access repository [7].

M_S [MA/m]	A_{ex} [J/m^3]	K_U [MJ/m^3]
0.75	1.8×10^{-11}	1.00

Table 1: Micromagnetic Parameters exctracted from magnetometry used in model.

3. Multilayer Simulations

3.1 Micromagnetic Parameters

All but the DMI vector strength are extracted / calculated from SQUID values. The DMI strength was chosen to be a value such that labyrinthine domains would form. The values used are shown in table 1.

Exchange stiffness was calculated from fitting a magnon dispersion relation in thin films. We here use a form based on the equations outlined in the supplementary section of Huang *et al.* (2025) [3]:

$$m_z(T) = 1 + \frac{1}{k_B T}\frac{8\pi}{L_z}\frac{2g\mu_B}{M_S D}\sum_{m=0}^{N-1} \ln\left[1 - \exp\left(\frac{g\mu_B B_0}{k_B T} - \frac{D}{k_B T}\left(\frac{m\pi}{(N-1)a}\right)^2\right)\right] \tag{2}$$

where L_z, D, B_0 and a are the fitted values corresponding to film width, magnon stiffness, external field and lattice parameter respectively. We use the conversion $A_{\mathrm{ex}} = \frac{DM_S}{2g\mu_B}$ to obtain the exchange stiffness. M v T relations are fitted for both multilayers on wide-terraced Bi_2Se_3 with Ta(2.0 nm) and Mo(1.0 nm) buffers and are shown in Fig. 9. Using Bumps fitting, a factor of ~ 4 difference is found between them. Both fits achieve satisfactory chi-squared values. For simulations, the values extracted from the sample on the Ta buffer were chosen. Mumax3 uses uniaxial magnetic anisotropy, K_U where $K_U = K_{\mathrm{eff}} + \frac{1}{2}\mu_0 M_S^2 = K_{\mathrm{eff}} + 0.34$ MJ/m^3

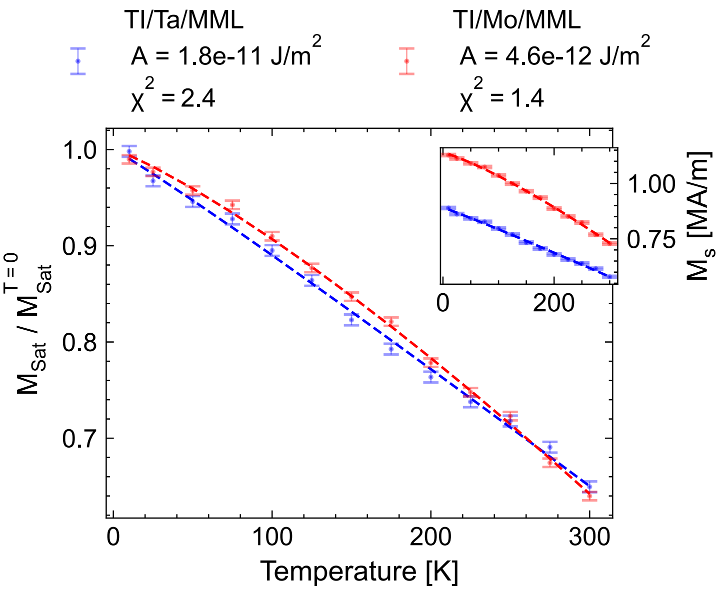

Figure 9: Fitted Thin film M v H models to SQUID-VSM data shown for two multilayer structures grown on wide-terraced Bi_2Se_3.

3.2 Micromagnetic Model

Simulations composed of 6, 0.6 nm magnetic layers separated by non magnetic spaces 1.2 nm layers thick and were simulated using mumax3 [6, 5]. Discretisation in x, y is set to 2.5 nm to be below the key lengthscales of the wall-width, $\delta = \sqrt{\frac{A}{K}} \sim 5$ nm and exchange length, $l_{\text{ex}} = \sqrt{\frac{A}{\mu_0 M_s^2}} \sim 5$ nm. The model used can be found in the open access repository [7].

The DMI vector strength D was increased such that a labyrinthine maze domain state formed reliably through lowering domain wall energy. This was found to be D = 5 meV/m^2. This is likely multiple times higher than the true value and the domain nucleation energy in the true films will instead be lowered by the presence of grains and disorder however this is beyond the scope of this paper. The simulated domains are an order of magnitude than those observed ($\sim 10 - 30$ nm instead of $\sim 400 - 600$ nm) however are included as a test that arbitrary spin textures couple magneto-statically which they are observed to do so.

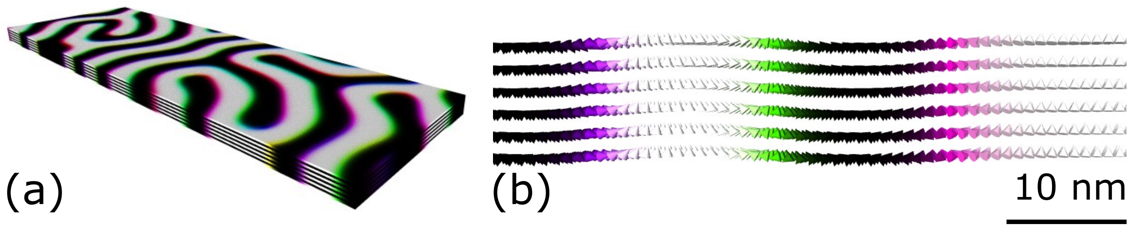

Figure 10: (a) DMI-induced spin textures coupling magnetostatically throughout the multilayer; (b) cross sectional view.

References

[1] D. Foreman-Mackey. corner.py: Scatterplot matrices in python. *The Journal of Open Source Software*, 1:24, 2016.

[2] A. Glavic and M. Björck. Genx 3 : the latest generation of an established tool. *J. Appl. Cryst.*, 55:1063, 2022.

[3] L. Huang, J. Barker, L. Kailas, S. Hait, S. D. Connell, G. Burnell, and C. H. Marrows. *Phys. Rev. B*, 113:014428, 2026.

[4] B. B. Maranville, P. Kienzle, R. Sheridan, A. J. Caruana, J. Borreguero, A. Nelson, D. P. Hoogerheide, A. Book, M. Blackman, P. P. Balakrishnan, and R. Ghose. reflectometry/refl1d: v1.0.0, 2025.

[5] J. Mulkers, B. Van Waeyenberge, and M. V. Milošević. Effects of spatially-engineered Dzyaloshinskii-Moriya interaction in ferromagnetic films. *Phys. Rev. B*, 95:144401, 2017.

[6] A. Vansteenkiste, J. Leliaert, M. Dvornik, M. Helsen, F. Garcia-Sanchez, and B. Van Waeyenberge. The design and verification of Mumax3. *AIP Advances*, 4:107133, 2014.

[7] B. A. Brereton, S. Hait, A. Yagmur and C. J. Kinane, F. Maccherozzi, M. Conroy, S. Sasaki, T. A. Moore, S. S. Dhesi, S. Langridge and C. H. Marrows, Research Data Leeds, https://doi.org/TBD, 2025